# Laser-Based Multiparameter Measurements in a Jet Engine Burner

G. Grünefeld*
*University of Bielefeld, 33615 Bielefeld, Germany*
V. Beushausen†
*Laser-Laboratorium Göttingen, 37077 Göttingen, Germany*
and
A. Brockhinke‡ and P. Andresen§
*University of Bielefeld, 33615 Bielefeld, Germany*

**Novel ultraviolet laser-based multidimensional measurement techniques were applied to the burner exit of a $H_2$–air jet engine. Two-dimensional Rayleigh scattering and one-dimensional Raman scattering were used to measure the mean temperature field, the distributions of the majority species $H_2$, $O_2$, $H_2O$, and $N_2$, and the turbulence intensity distribution $\sigma_T/T$ in the burner exit plane. The wealth of data allows are elucidation of the turbulent mixing and combustion processes inside the burner. For example, the majority species distributions show that unburned $H_2$ occurred in certain regions in the burner exit plane that were essentially free of $O_2$ and vice versa. This pattern was constant in time. This means that certain flow structures in the burner caused rich mixing in some areas and lean mixing in others, and it explains why overall combustion was not complete in this particular burner.**

## Introduction

LASER diagnostic techniques undoubtedly have a high potential for nonintrusive molecular species, temperature, and velocity measurements with high spatial and temporal resolution in combustion and flow systems. Laser-induced fluorescence (LIF), coherent anti-Stokes Raman spectroscopy (CARS), Raman scattering, and Rayleigh scattering are the most commonly used techniques for species and temperature measurements. Raman scattering has the unique advantage of being able to provide the densities of all majority species and the temperature using a single laser beam. It is now possible to measure these quantities with one-dimensional spatial resolution (along a line) by using a spatially resolving optical multichannel analyzer (SROMA) as the detector.[1−3] It is demonstrated in this paper that a large number of one-dimensional measurements yield quasi-two-dimensional multispecies concentration and temperature fields at the burner exit of an $H_2$–air jet engine.

Because Raman (as well as Rayleigh) scattering intensities increase with the fourth power of the scattered laser frequency, this application of Raman scattering is possible given the availability of deep uv laser sources. Although this fundamental behavior was well known, there have been very few applications of deep uv Raman and Rayleigh scattering to flames[1−5] and to flowfield diagnostics and mixing problems.[6−9] The measurements presented in this paper are one of the first successful applications of one-dimensional Raman (and Rayleigh) scattering in a realistic combustion system.[10] It is demonstrated that these improved measurement techniques can, indeed, be used as a tool for the development of combustion systems.

It is also demonstrated that a combination of Raman, Rayleigh scattering, and LIF techniques is particularly useful for applied combustion diagnostics, because it yields temperature (via Rayleigh), majority species (via Raman), and minority species (via LIF) information. All three techniques can be applied simultaneously using a single laser beam and an SROMA system. An example is given subsequently.

Rayleigh scattering yields the total density in particle-free media, so that the flame temperature can be derived through the ideal gas law in atmospheric flames.[2] Different Rayleigh cross sections of different species are taken into account using temporally averaged majority species distributions measured by Raman scattering. This yields precise mean temperature fields. Rayleigh scattering measurements can be performed with two-dimensional spatial resolution even on a single laser shot basis and even with a large object-detector distance (1–2 m) if deep uv wavelengths are applied, as in this work. This yields approximate two-dimensional temperature fields with a temporal resolution of the order of 10 ns (laser pulse length). The mean temperature field can be deduced from a large number of single-shot measurements as will be demonstrated. The turbulence intensity field (temporal temperature and species variations) can also be obtained from single-shot Rayleigh measurements.

Two-dimensional Rayleigh scattering and one-dimensional Raman scattering techniques were applied to an $H_2$–air jet engine burner to obtain the temperature field and the distributions of the majority species $H_2$, $O_2$, $H_2O$, and $N_2$ at the burner exit for characterization of the nozzle entry conditions. The burner was located at the DLR, German Aerospace Research Establishment, Cologne. This burner belongs to a prototype $H_2$–air jet engine. The nozzle was removed for the measurements to gain optical access. Air-breathing jet engines are being developed for advanced aerospace propulsion systems.[12] With two different experimental setups (one and two dimensional) the measurements were performed within a five days measurement campaign in 1994. The experiments were also done to demonstrate the capabilities of the novel measurement technique.

Although temperature and species concentration determination from Raman and Rayleigh scattering intensities is essentially easy, it will be seen that a number of difficulties arose in this particular application. It is generally much more difficult to obtain precise quantitative data in a turbulent atmospheric flame than in cold (precombustion) media,[6−9] basically because of 1) smaller signal levels, 2) stronger laser-induced (predissociative) fluorescence [LI(P)F] interferences for $H_2$, $O_2$, and $H_2O$ (will be compared), and 3) averaging errors due to turbulence.[11] In addition, the measurements suffered from hostile conditions at this test stand, such as mechanical vibrations of the setup. Thus, it is necessary to discuss these sources of error extensively and to develop appropriate data evaluation procedures to avoid quantitative measurement errors.

*Doctor Scientist, Department of Physics, Universitätsstrasse 25.
†Doctor Scientist, Combustion Research, Hans-Adolf-Krebs Weg 1.
‡Graduate Student, Department of Chemistry, Universitätsstrasse 25.
§Professor, Department of Physics, Universitätsstrasse 25.

## Experiment

The $H_2$–air burner and the test stand are described in more detail elsewhere.[12] The burner geometry is outlined in Fig. 1a. In this burner, hydrogen is injected with high pressure through 54 orifices in 6 injection fingers into the air flow. Combustion occurs before mixing is complete and a considerable fraction of unburned hydrogen and oxygen is present (in the present state) at the burner exit. The Laval nozzle was removed to obtain optical access, and the measurements were done in the turbulent free jet 5 cm behind the burner exit plane. The rectangular burner exit opening was $250 \times 125$ mm. The burner was operated with 10-g/s hydrogen throughput ($\Phi = 0.9$) in the measurements presented subsequently. The free-jet velocity was subsonic (some 80 m/s).

Two slightly different arrangements were used in the two-dimensional Rayleigh scattering and the one-dimensional Raman measurements, respectively. The same tunable KrF excimer laser (Lambda Physik, 0.2 J/pulse at $\approx 248$ nm) and an intensified slow scan charge-coupled device (CCD) camera (LaVision) were used in both cases. For the one-dimensional Raman measurements, an additional SROMA system consisting of a CCD camera and an imaging spectrograph (Oriel) was used. The basic setup is outlined in Fig. 1b. It can be seen that there was an angle of 30 deg between the detector axis and the burner axis because the camera system could only be practically located beside the burner exhaust. Accordingly, the camera system was not perpendicularly oriented with regard to the laser beam. (The resulting distortion of the images was tolerable.) A three-dimensional adjustable arrangement was used to move the camera system and the laser beam optics, so that measurements could be performed, in principle, in all regions of the burner exhaust and the ambient air. Two-dimensional Rayleigh measurements were done at 18 positions in order to cover the whole exit plane. On the right-half of the exit plane 32 one-dimensional Raman scattering measurements were carried out. Figure 2 shows schematically the burner exit (inner rectangle), the positions of the 18 two-dimensional Rayleigh scattering measurements (in the outer rectangle) and the positions of the Raman measurements (additional horizontal lines on the right-half).

The laser beam was formed to a sheet ($1 \times 24$ mm) using a telescope consisting of two cylindrical lenses in the case of the two-dimensional Rayleigh measurements (as shown in Fig. 1b). A
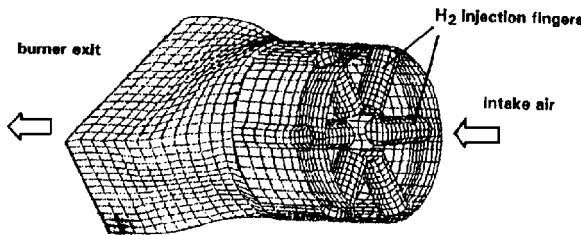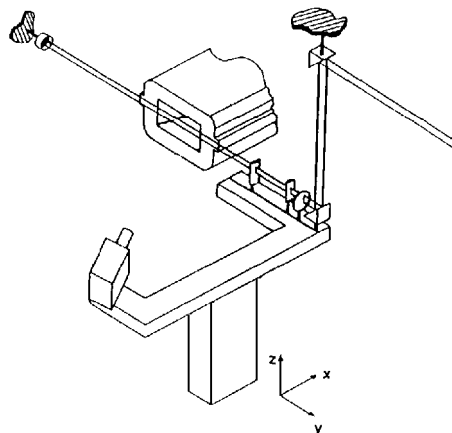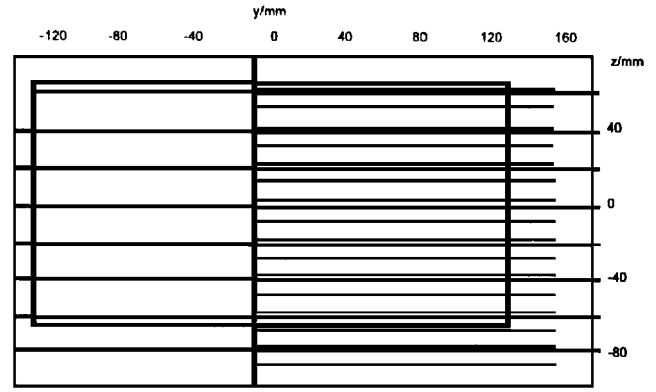


**Fig. 2   Measurement positions of 18 two-dimensional Rayleigh scattering and 32 one-dimensional Raman scattering (additional horizontal lines on the right side) measurements at the burner exit (inner rectangle).**

spherical lens ($f = 2$ m) was used to form a focused laser beam ($2 \times 2$ mm profile) in the Raman measurements. The detector–probe volume distance was about 1.4 m. The observed section of the laser beam as determined by the detector size and the imaging optics was 18 cm in the case of the Rayleigh measurements and 8 cm in the Raman measurements, respectively. Two dielectric laser mirrors (45 deg, $248 \pm 20$ nm) were used to transmit essentially only the laser wavelength to the camera in the two-dimensional measurements. It was demonstrated in a flat flame burner (McKenna), which was used also for calibration purposes, that this filter sufficiently suppressed other laser-induced emissions (in particular, LIPF signals from OH and $O_2$ even on resonance[13]). A 0-deg, $248 \pm 10$ nm dielectric filter was used to suppress the Rayleigh line in the Raman measurements. The filters were mounted directly in front of the camera or the spectrograph, respectively. Spherical quartz lenses with a diameter of 5 cm were used in both cases for imaging.

## Majority Species Measurements via Raman Scattering

The SROMA detection system used in the one-dimensional measurements covered an emission wavelength range from 240 to 285 nm. With this setup, a number of different laser-induced emissions were detected simultaneously with one-dimensional spatial resolution: 1) Rayleigh scattering at 248 nm (the laser wavelength); 2) vibrational Raman emissions from $O_2$ at 258 nm, $N_2$ at 264 nm, $H_2O$ at 273 nm, and $H_2$ at 277 nm; and 3) LIPF from $O_2$ at three different wavelengths (258, 267, and 277 nm). In principle, the majority species densities $\rho_i$ ($i = O_2, N_2, H_2O, H_2$) can be obtained from the intensity of the Raman emission lines $I_i$, provided that the slightly temperature-dependent scattering crosssection $\sigma_i^{(R)}$ is known, through

$$I_i = c \sigma_i^{(R)} \rho_i \qquad (1)$$

where $c$ is the overall detection efficiency, which depends on the laser power, the detection solid angle, polarization properties, and the efficiency of the detection system consisting of spectrometer, Rayleigh rejection filter, and intensified CCD camera. However, difficulties often arise in the determination of the pure Raman signal intensities, $I_i$ due to interferences, in particular from LIF emissions that occur at the same wavelengths as the Raman emissions. LIPF emissions from $O_2$ and OH are particularly severe in hydrogen flames with KrF laser excitation.[13] Thus, tunable excimer lasers are applied for Raman measurements to avoid LIPF emissions by tuning the laser wavelength between the LIPF excitation lines.[1-5] This usually works well in the case of OH LIPF using the KrF laser, i.e., OH LIPF can be effectively avoided. In contrast, a nonvanishing amount of $O_2$ LIPF emissions is usually obtained in hydrogen flames with the KrF laser, and $O_2$ LIPF interferes with $O_2$ Raman and $H_2$ Raman emissions (already mentioned). It is possible in principle to discriminate Raman (and Rayleigh) emissions against unwanted $O_2$ LIPF using polarization techniques.[3,10,14] Unfortunately, it is not possible at the present to use these polarization techniques with a 30-deg



**a) Geometry of the burner of a jet engine (DLR Cologne)**

**b) Experimental setup at the burner**

**Fig. 1   Laser sheet forming optics for two-dimensional Rayleigh scattering measurements.**

angle between detector and laser beam as in this application. Thus, it was necessary to develop an alternative data evaluation method for discrimination of the interfering $O_2$ LIPF emissions to obtain the densities of $H_2$ and $O_2$. The basis of this method is that the emissions of three different vibrational transitions of $O_2$ were recorded simultaneously with the SROMA system, as mentioned earlier. The emissions at 258 and 277 nm interfere with the $O_2$ and $H_2$ Raman lines, respectively, but the emission at 267 nm is interference free. Thus, it is possible, in principle, to determine the intensities of the interfering $O_2$ LIPF emissions from the interference-free emission at 277 nm, because the emissions occur in a constant intensity proportion (which is essentially given by the Franck–Condon factors[10]). The appropriate factors were determined in a calibration measurement in the postflame region of a flat flame burner (McKenna). The $H_2$–air burner was operated lean or rich in order to obtain all three $O_2$ LIPF emissions interference free in different measurements. This is possible because traces of $O_2$ can be detected by LIPF under rich conditions, when the Raman scattering intensity of $O_2$ is negligible. The measurements in the flat flame burner, which were done shortly before or after the jet engine burner operated, were also used to adjust the laser wavelength between the excitation lines of $O_2$ and OH and to determine the relative Raman scattering cross sections of the majoriy species.

It will be seen that this method for discrimination of interfering $O_2$ LIPF emissions worked fairly well in the case of $H_2$, but caused considerable errors in the case of $O_2$. (This is mainly because most of the unburned $O_2$ and $H_2$ occurred in different regions, as will be seen.) The method is inaccurate because the $O_2$ LIPF emissions were usually stronger than the Raman emission resulting in a small signal on a large background. Thus, it was not possible to derive the mole fractions $\chi_i$ of the majority species $i$ directly from the densities of all majority species $j$ via $\chi_i = \rho_i / \Sigma \rho_j$, because the $O_2$ density was too inaccurate. (This underlines the importance of the application of advanced polarization techniques in the future as proposed elsewhere.[10, 13])

Additional problems arose from mechanical vibrations of the components of the setup when the burner was operating. This was particularly severe in the case of the one-dimensional measurements because slight dealignment of the laser beam with regard to the SROMA detector can cause large signal loss. Thus, it was necessary to derive the mole fractions of the majority species via ratios of Raman signals, i.e., in a relative measurement, so that the overall detection efficiency $c$ cancels out

$$I_i / I_j = (\sigma_i^{(R)} / \sigma_j^{(R)})(\rho_i / \rho_j) \tag{2}$$

Also note that the temperature dependence of the ratios of cross sections $\sigma_i^{(R)} / \sigma_j^{(R)}$ is smaller than the aforementioned temperature dependence of the Raman cross section of a single species $\sigma_i^{(R)}$, because the temperature dependence is similar for all species $i$ (Ref. 10). Thus, it was assumed in the data evaluation procedure that $\sigma_i^{(R)} / \sigma_j^{(R)}$ is independent of the temperature. (Errors occur from different vibrational energy quanta, line width effects, and contributions from different vibrational modes in the case of $H_2O$, but it can be estimated that the resulting error is smaller than other occurring errors due to LIPF interferences.[10]) Thus, data evaluation via ratios of cross sections essentially eliminates the necessity to calibrate the Raman signals for different temperatures, provided that the concerned temperature range is not too large.

The mole fractions of $N_2$, $H_2O$, and $H_2$ were determined from the $I_i / I_{N2}$ ratios using a data evaluation procedure that is given elsewhere.[10] It was mentioned earlier that the oxygen Raman intensity could not be determined accurately from the $O_2$ Raman emission due to interferences. Note that the Raman signal intensities of different species are not only proportional to their mole fraction but also to their scattering cross sections, etc. Therefore, $[O_2]$ was more accurately deduced from the sum of the other majority species,

$$[O_2] = 1 - [N_2] - [H_2O] - [H_2] \tag{3}$$

Figure 3 shows the $N_2$ and $H_2O$ concentration distributions averaged over 960 laser shots on the right side of the burner exit (compare Fig. 2). The combination of a large number of line measurements results in quasi-two-dimensional images.
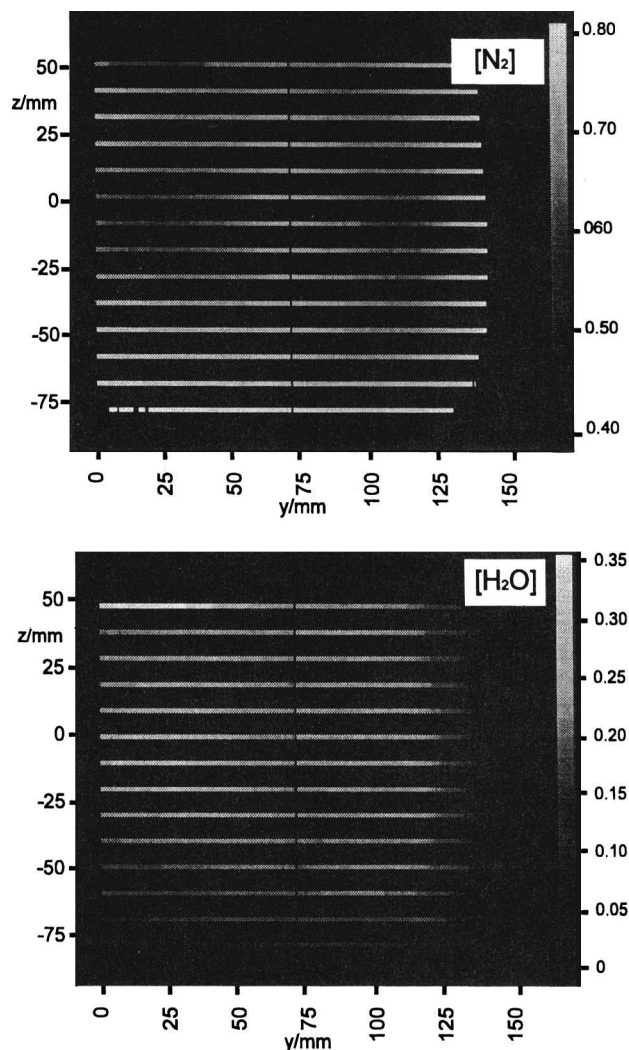


**Fig. 3   Species concentrations of nitrogen and water on the right-hand side of the burner exit plane; the z axis corresponds to the concentration.**

It is the main feature of these distributions that the mixing zone of the exhaust gas and the ambient air can be clearly seen, particularly in the $H_2O$ concentrations (see also the $O_2$ distribution in Fig. 4). This suggests that the structure of the temperature field is affected by mixing of the freejet with cold ambient air, which will be discussed in more detail in the following section.

It is probably the most important objective of the species concentration measurements to determine the regions where unburned hydrogen and oxygen occur at the burner exit, because it is important to improve the completeness of combustion before the gas enters the Laval nozzle. Figure 4 shows the averaged distributions of $H_2$ and $O_2$ in the right-half of the burner exit plane. The $O_2$ concentration within the hot regions ($T > 900$ K) can also be derived in a qualitative way from the simultaneously detected $O_2$ LIPF. Cold ambient oxygen cannot be observed using this detection method because it works via highly excited initial states of vibration ($v'' = 6$ and 7) (Ref. 13). In this case the data cannot be quantified due to two effects: 1) the strong temperature dependence and 2) excitation by the broadband portion of the laser radiation.[10] However, the LIPF emission is very sensitive to traces of unburned oxygen in the exhaust gas, and the resulting distribution corroborates the $O_2$ distribution that was derived from the sum of the other majority species in Fig. 4.

Unburned $H_2$ occurs in regions that are essentially free of $O_2$ and vice versa. This implies that combustion is incomplete in this burner mainly because poor mixing of $H_2$ and $O_2$ results in large spatial structures of nonstoichiometric mixture. These large structures are essentially constant in time (over a long time scale), because they
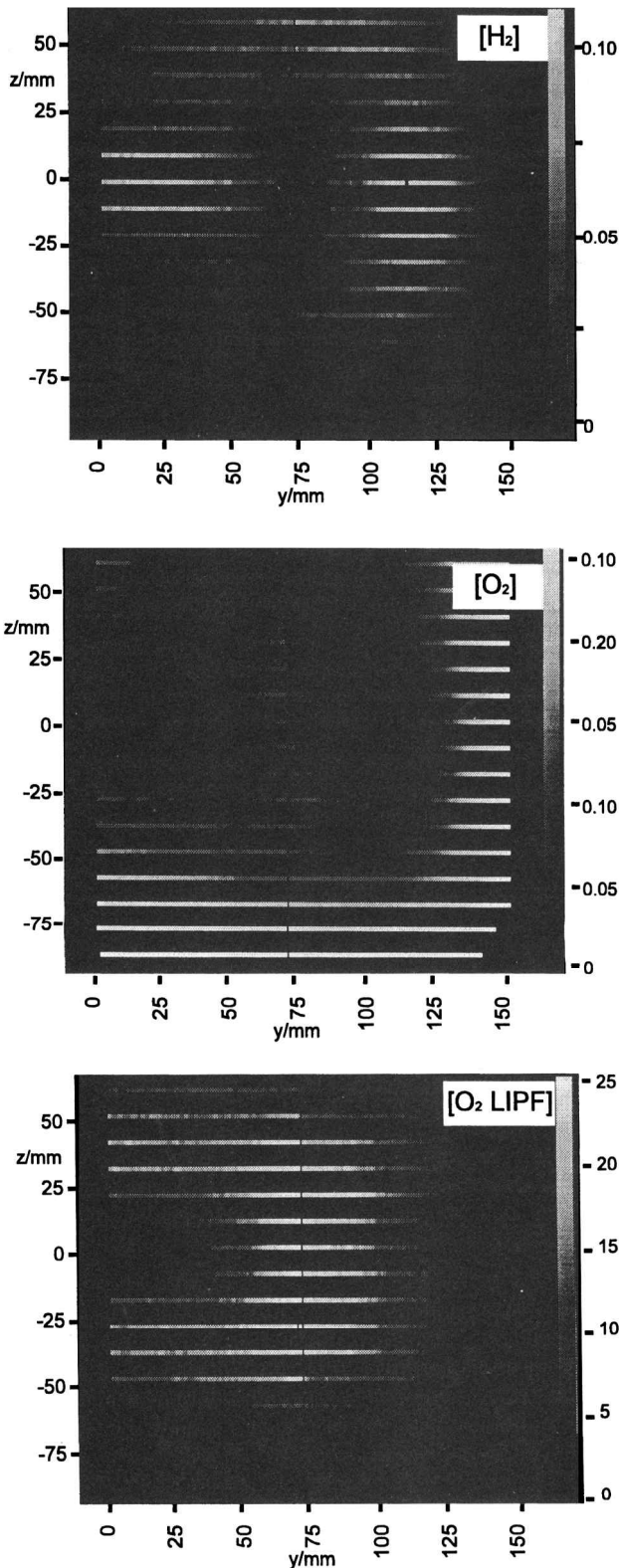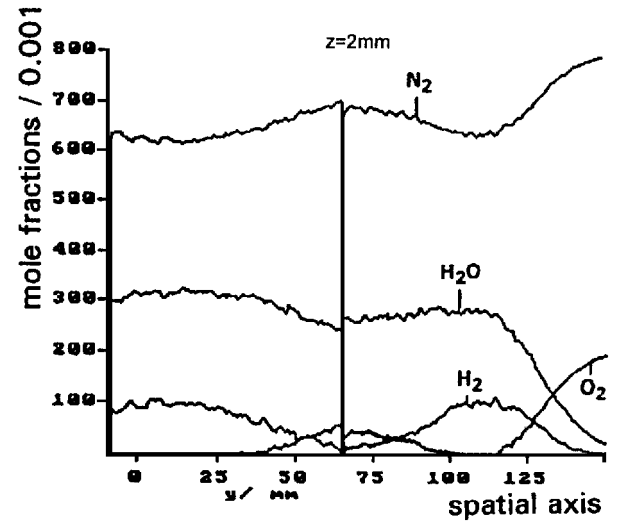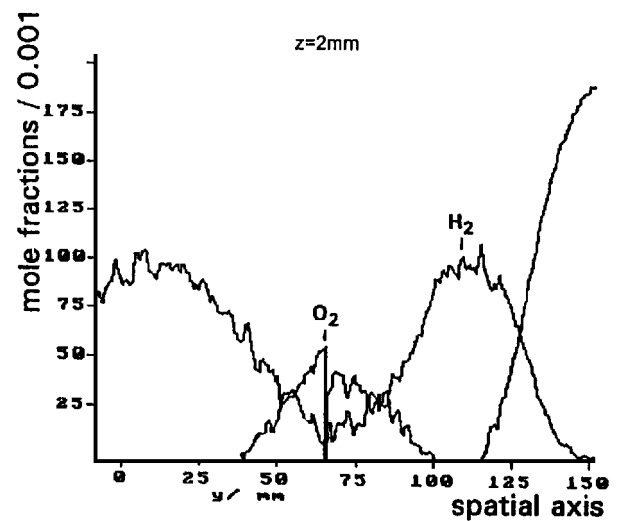
Fig. 4 Species concentrations of hydrogen and oxygen, and the oxygen LIPF distribution on the right side of the burner exit plane; the *z* axis corresponds to the concentration.



a) Majority species



b) Hydrogen and oxygen

Fig. 5 Species concentrations at $z = 2$ mm.

can still be observed by averaged measurements (even though there may be some high-frequency fluctuations in the $H_2$ concentration). Temporal averaging explains why there is some overlap in the distributions of $H_2$ and $O_2$. The existence of some overlap does not necessarily mean that unburned $H_2$ and $O_2$ occurred at the same place and the same time.

It can be seen that $H_2$ is mainly detected in the center of the burner exit (up to some 10%) and near its right edge. These structures cannot

be easily explained by the hydrogen injection geometry. This will be further discussed in the last section.

The occurring structures of nonstoichiometric combustion also explain why there are modulations in the $H_2O$ and $N_2$ concentrations within the exhaust gas region. Rich or stoichiometric combustion leads to a $[N_2]/[H_2O]$ ratio of 2/1, whereas $[N_2]/[H_2O] > 2$ after lean combustion. Concentration profiles at $z = 2$ mm from Fig. 3 are summarized in Fig. 5 (Fig. 5b shows the $H_2$ and $O_2$ profiles with a different scale). It can be seen in Fig. 5 that $[N_2]/[H_2O]$ equals 2 near $y = 0$, i.e., in the center. This corroborates that combustion is rich or at least stoichiometric in this region. The ratio of 2 is not precisely matched at $y \approx 110$ mm, where combustion was also rich, as indicated by the $H_2$ concentration. This can be explained by mixing with ambient air in this region.

The measurement errors of the concentration profiles are different for the different majority species. The error in $[N_2]$ and $[H_2O]$ is dominated by calibration errors mainly due to pixel-dependent gain and detection solid angle effects. Such effects are extensively discussed elsewhere.[9,10] For example, it can be seen in Fig. 3 that the horizontal $[H_2O]$ and $[N_2]$ profiles are not continuous at $y = 65$ mm, i.e., at the link of two neighboring measurement positions. The differences in the pixel-dependent gain of the left and right edges of the spatial range of the detector were not precisely eliminated by the calibration procedure. The resulting error can be estimated to be 3–5% for $[N_2]$ and $[H_2O]$. The error in $[H_2]$ is dominated by inaccurate discrimination of LIPF interferences as already discussed and is roughly 20%. It turned out that $[O_2]$ could

be precisely derived from the sum of the other majority species, as seen earlier. For example, summation in oxygen-free regions results in $[N_2] + [H_2O] + [H_2] = 1.00 \pm 0.02$, i.e., it differs only 2% from unity. This suggests that the error of $[N_2]$ and $[H_2O]$ is, indeed, on the order of a few percent.

It turned out that the repeatability of the concentration measurements was good even with reduced shot numbers. The data given were averaged over 960 shots. Figure 6 shows the resulting data from two measurements with 320 shots each. It is seen that the quantitative repeatability is better than 95% for $[N_2]$ and $[H_2O]$, and at least 90% for $[H_2]$ and $[O_2]$, respectively.

It was not clear what caused the occurring structures of unburned $H_2$ and $O_2$ at the burner exit. The occurring pattern (interpreted as a symmetric ring structure) and the injection geometry of the burner are roughly outlined in Fig. 7. (Symmetry with regard to the vertical middle axis is suggested by the temperature measurements as seen in the following section.) Obviously, the six $H_2$ injection



**a) Nitrogen and water at z = 2 mm using 320 laser pulses in each measurement**



**b) Hydrogen and oxygen**

**Fig. 6   Repeatability of concentration profiles.**



**Fig. 7   H$_2$ injection geometry in the burner and the observed distributions of unburned H$_2$ and O$_2$ at the burner exit shown schematically.**

fingers are not reflected in the unburned $H_2$ and $O_2$ distributions. It is particularly surprising that unburned $H_2$ occurs in the center where no $H_2$ is injected.

### Temperature Field via Two-Dimensional Rayleigh Scattering

The temperature field can be measured by two-dimensional Rayleigh scattering in such applications, because the intensity of the Rayleigh signal, $I_R$, is proportional to the total density $\rho$ of the molecules in the probe volume, and the ideal gas law can be applied, providing that the pressure is known (here, 1 bar $\pm 2$ mbar):

$$T \propto 1/\rho \propto 1/I_R \qquad (4)$$

It is demonstrated elsewhere that small density (or temperature) differences of 0.5–1%, in principle, can be detected using the two-dimensional Rayleigh technique.[9] However, it is crucial to determine the effective Rayleigh scattering cross section $\sigma_{\text{eff}}$ in order to quantify the results.[2] For this purpose, the mole fractions, $\chi_i$ of the majority species are generally necessary because different species $i$ yield different Rayleigh scattering cross sections $\sigma_i$. The Rayleigh scattering signal at constant pressure can be expressed as

$$I_R = \frac{(\Sigma \chi_i \sigma_i)cl}{T} \equiv \frac{\sigma_{\text{eff}} cl}{T} \qquad (5)$$

This equation defines the effective Rayleigh scattering cross section where $cl$ is a calibration constant that is determined via calibration of the measurement system in a well-characterized medium; for example, in room air under normal conditions, as in this work. For determination of $\sigma_{\text{eff}}$ the average mole fractions $\chi_i$ of all of the majority species, $H_2$, $O_2$, $H_2O$, and $N_2$, were measured as described in the preceding section.

Other problems using Rayleigh scattering may arise from surface and/or Mie scattering. Appropriate filter techniques for discrimination of these interferences are not yet available at the excimer wavelengths applied in theses studies. However, it turned out that stray light from the burner surface only occurred in certain small regions of the images (discussed in the following). Mie scattering, most probably from water droplets, was severe only at a certain measurement position (discussed in the following). In most regions of the measurement plane only a few single-shot Rayleigh scattering images had to be eliminated because of too severe Mie scattering.

Absorption of the laser beam in the probe volume can cause problems. This would affect the calibration constant. In this work the laser wavelength was tuned between the absorption lines of $O_2$ and OH before the actual measurement, so that it can be assumed that no considerable absorption occurred.

It is generally necessary to perform single-shot measurements in turbulent media, because otherwise averaging errors may occur.[11] This was achieved by the two-dimensional Rayleigh technique. The single-shot images were converted to single-shot temperature fields as will be described. The two-dimensional single-shot temperature distributions were subsequently averaged to obtain the mean temperature distribution. The spatial distribution of temperature fluctuations was also calculated from these single-shot images. A single-shot precision of the Rayleigh scattering signals of $<3\%$ due to photon statistical noise[9] was achieved for each detector element with a spatial resolution of 1.5 mm.

At present, it is not possible to perform single-shot one-dimensional Raman scattering measurements over a spatial detection range of several centimeters in atmospheric flames due to small signal levels, even though uv wavelengths are used (see Introduction).[10] Thus, one-dimensional Raman scattering measurements were averaged over an appropriate number of laser shots, so that an averaged, effective Rayleigh scattering cross section could be determined. It is discussed subsequently that the resulting error of the temperature field and the majority species distributions is small and therefore negligible in comparison to other sources of error.

At each measurement position, 50 single-shot Rayleigh scattering images were recorded. It turned out that this was sufficient to obtain a reproducible mean temperature distribution despite the turbulence (discussed subsequently). The single-shot images were converted to temperature fields using calibration images acquired in room air
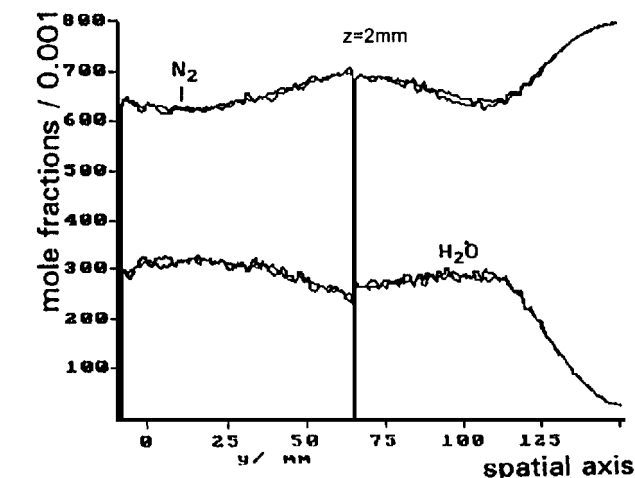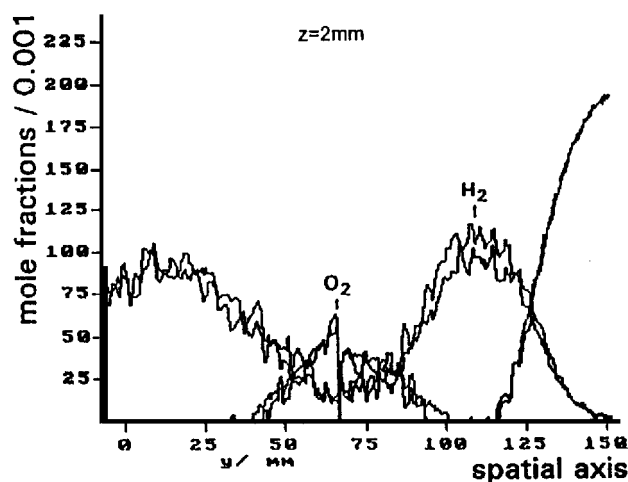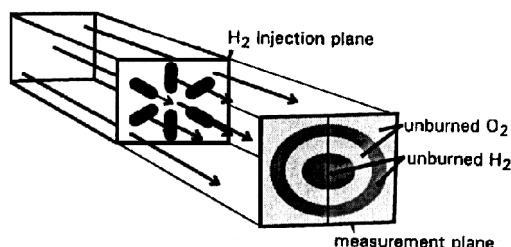
(ra) with known temperature, $T_{ra}$. This calibration procedure for each detector element is demonstrated in more detail elsewhere.[9]

The temperature data given in the following were calculated under the assumption that the effective Rayleigh scattering cross section is equal to that obtained in room air

$$\sigma_{eff} \approx \sigma_{ra} \qquad (6)$$

because calibration of the images via the Raman measurements was only possible at distinct line positions (this correction will be applied at the end of this section). The error introduced by this assumption [Eq. (6)] is smaller than about 10%, as will be seen in the following discussion. It was seen in the preceding section that the measurements were made in a region of the combustor where combustion was locally (not overall) approximately complete, but considerable variations in the gas composition occurred across the field of view because of spatial variations in the stoichiometry.

The error due to these changes in the gas composition without the correction of the Rayleigh scattering cross section can be estimated as follows. The relative Rayleigh scattering cross sections for the different species are given in Ref. 2. Only the relative cross section of $H_2$ differs substantially from that of air. Consequently, the error due to Eq. (6) is dominated by the uncertainty in the $H_2$ concentration. It was seen in the preceding section that (on average) up to 10% $H_2$ occurs in certain regions at the burner exit. Under the assumption that the $O_2$ concentration is negligible in these regions, which was corroborated by the measurements, the effective Rayleigh scattering cross section of the exhaust gas (consisting of 10% $H_2$, 30% $H_2O$, and 60% $N_2$ as calculated) equals $\sigma_i/\sigma_{ra} = 0.87$. In contrast, the assumption of complete combustion of a mixture with $\Phi = 0.9$ corresponding to the overall $H_2$/air throughput would result in exhaust gas that consists of 68% $N_2$, 31% $H_2O$, and 1% $O_2$. This would yield an effective Rayleigh scattering cross section of $\sigma_i/\sigma_{ra} = 0.94$. Consequently, the assumption of overall complete combustion (as far as possible) at the burner exit would result in a temperature error of 7%. It will be seen that most of the unburned hydrogen occurred in spatial regions where the temporal variations in the temperature field were rather small (10–20% standard deviation from shot to shot), so that the temporally averaged concentration measurements via Raman scattering yield a high precision (less than 5% relative error) for the correction of the effective Rayleigh scattering cross section.

The largest concentration gradients in these measurements result from mixing of exhaust gas and ambient air. It can be calculated from the Rayleigh scattering cross sections[2] that this would result in an error of 6% because the effective Rayleigh scattering cross section of pure exhaust gas (from combustion at $\Phi = 0.9$) equals $\sigma_i/\sigma_{ra} = 0.94$ as already seen. These calculations underline the importance of the correction of the effective Rayleigh scattering cross section. However, it will be seen that the correction of the effective Rayleigh scattering cross section on the basis of the Raman scattering measurements does not change the major features of the temperature field obtained without this correction.

Figure 8 shows a number of resulting single-shot temperature distributions. The spatial area extends over $20 \times 170$ mm. The images were recorded at the $z = \_60, \dots, \_40$ mm position. The temperatures were converted to gray levels as shown.

Figure 9 shows the complete mean temperature field at the burner exit obtained by averaging over 50 single-shot temperature images in each position. Only in the uppermost position ($z = 60, \dots, 80$ mm) are a substantially smaller number of single-shot images available for averaging because about 90% of the raw images were eliminated due to strong Mie scattering. The Mie scattering in this position near the upper edge of the burner exit was caused by water droplets. The water in the exhaust gas condensated on the cold burner walls and was drawn into the freejet especially at the upper edge of the burner exit. The small number of underlying images in the uppermost positions is insufficient for averaging. (The measurement positions at $z = \_80, \dots, \_60$ mm were skipped due to a software error.)

The most important features of the two-dimensional mean temperature distribution are 1) the mean temperature peaks near the center, 2) the distribution is essentially symmetric with regard to both middle axes, 3) there is a waist in the temperature field near the
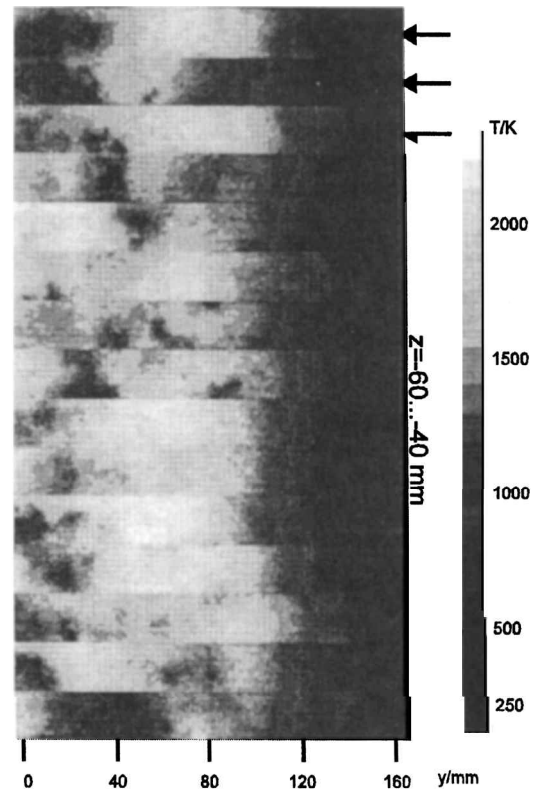


Fig. 8  Distributions of 30 single-shot temperature images from the burner exit at $z = \_60, \dots, \_40$ mm; $y$ range extends over about 165 mm (compare Fig. 2).
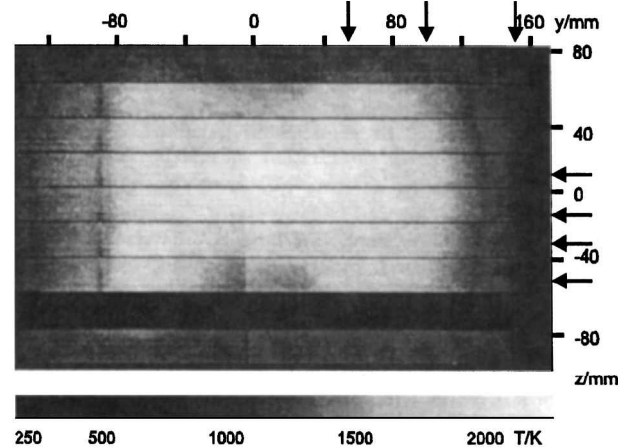


Fig. 9  Mean temperature field at the burner exit; temperatures were converted to gray levels.

vertical middle axis, and 4) there are no structures that reflect the $H_2$ injection geometry. The details of the temperature distribution can be seen more clearly in profile plots in Fig. 10 that were extracted from Fig. 9 at the positions marked by arrows. It can be seen in Figs. 9 and 10 that there is a temperature drop at $y \approx \_90$ mm in most measurement positions. This temperature drop is a measurement error, which is caused by stray light coming from the left edge of the burner exit (this was the only stray light present in these images).

It can be seen that the temperature profiles are not perfectly continuous at the edges of the measurement positions. These errors are caused by image defects and calibration errors. These are the main sources of error in these measurements (besides the aforementioned Mie and surface scattering problems), and they can be estimated to be 4–7% relative error. Obviously, photon statistical noise ($\lesssim 3\%$ in single shots) plays a negligible role, in particular for the mean
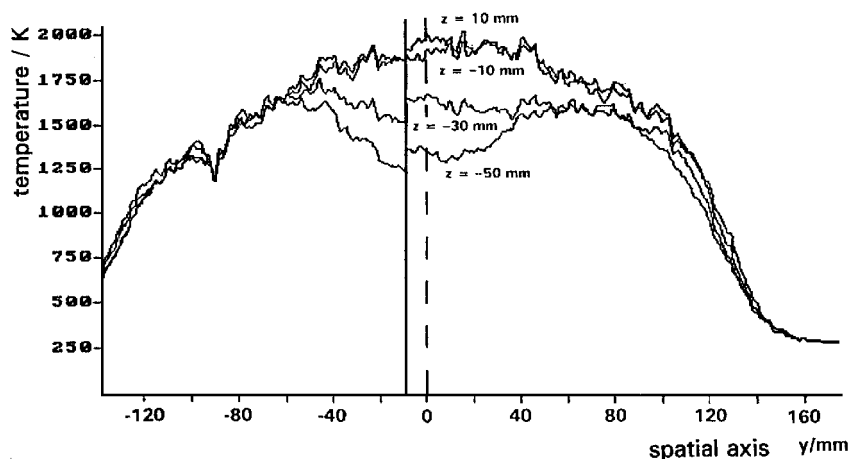
**Fig. 10   Horizontal mean temperature profiles extracted from the mean temperature field at the positions of the arrows in Fig. 9.**
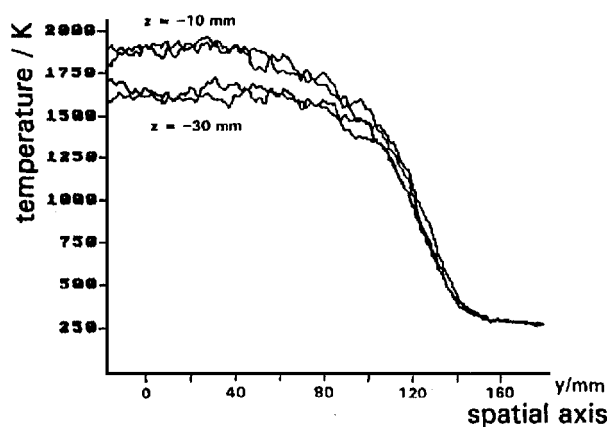


**Fig. 11   Repeatability of the mean temperature profiles from two different days at $z = \_10$ mm and $z = \_30$ mm, respectively.**



**Fig. 12   Mean temperature field from Fig. 9 corrected for the effective Rayleigh scattering cross section $\sigma_{\text{eff}}$; temperatures converted to gray levels.**

temperature field. Image defects are caused by a poor transmission function of the imaging and filtering optics. Calibration errors are mainly due to dealignment of the laser beam with regard to the camera system between the measurements in the jet and in room air, respectively. This was caused by mechanical vibrations when the burner was operating.

It turned out that the mean temperature field measured by two-dimensional Rayleigh scattering was highly reproducible. The measurement was repeated on a second day resulting in essentially the same distribution. Figure 11 shows horizontal profiles from different measurement days: one profile from each day at $z = \_10$ mm, and one from each day at $z = \_30$ mm, respectively. The deviations are smaller than the errors discussed earlier.

The mean temperature field was corrected for variations in the effective Rayleigh scattering cross section via the averaged concentration measurements of the majority species described in the preceding section. Thus, the error introduced by the averaging procedure of the Raman data must be considered. The Raman density data itself is only slightly influenced by averaging errors, because the Raman signals are roughly proportional to the density despite temperature fluctuations (the occurring temperature fluctuations will be quantified subsequently).[11] However, a temperature error may result from the nonlinear relation of temperature and the Rayleigh scattering signal via the effective cross section [Eq. (5)]. It was estimated earlier that the maximum error in the effective Rayleigh scattering cross section due to spatial variations in the gas composition is about 10%. Thus, it is reasonable to assume that temporal fluctuations in the Rayleigh scattering signal are also of the order of 10%. Obviously, the temperature hyperbola $T \propto 1/I_R$ can be approximated by a straight line over a 10% variation, which is roughly performed by averaging. The resulting error (due to integration) is much smaller
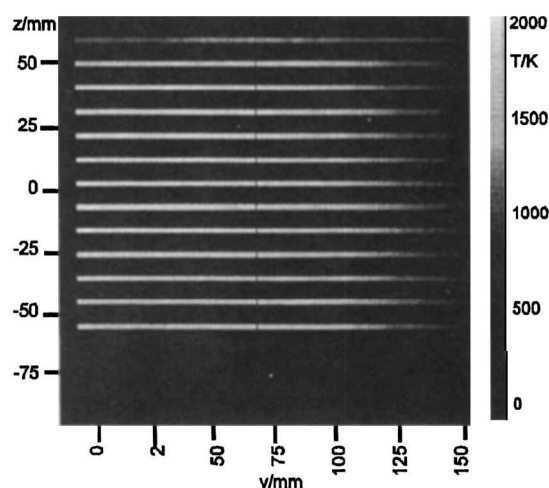
than 10%. Hence, other sources of error already discussed are much more important for the mean temperature field than the error due to averaging of the Raman scattering measurements.

The Raman scattering measurements were only done on the right-hand side of the burner exit due to restrictions in the measurement time (see Fig. 2). Thus, only the Rayleigh scattering temperature data on the right-hand side are quantified. Because it was demonstrated that the mean temperature field is essentially symmetric with regard to the middle axes, this approach was considered adequate for total flowfield characterization. Note that the burner operated repeatably from day to day, as already mentioned, so that the Rayleigh and Raman measurements from different days can be combined.

The raw temperature field in Fig. 9 was corrected for the effective Rayleigh scattering cross section on the distinct lines of the Raman measurements resulting in the temperature distribution in Fig. 12. The correction was less than 15%. It can be seen that the contour of the temperature field is essentially unchanged. The most important feature is that the peak in the center of the uncorrected temperature field decreased and the final distribution is more homogeneous in the central region (maximum $T \approx 1750\,\text{K}$). Some horizontal profiles extracted from Fig. 12 are given in Fig. 13. The temperature field will be further discussed.

It is also interesting to consider the temperature variability, i.e., the turbulence intensity $\sigma_T / T$, as a function of the $y/z$ position in the exit plane of the burner. This distribution can also be obtained from the single-shot temperature images. For this purpose, the standard deviation of the single-shot temperature data was calculated for
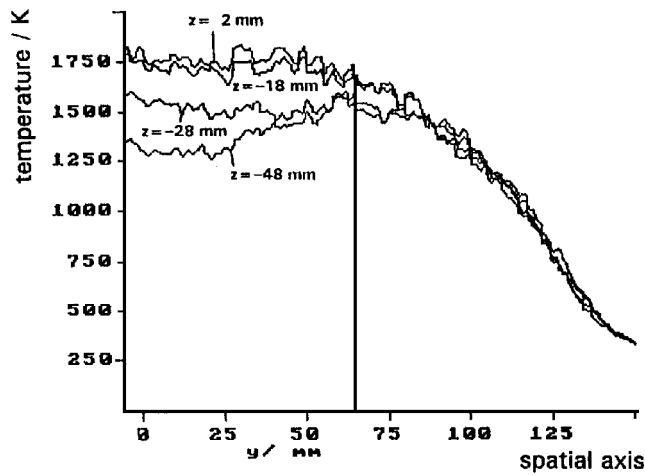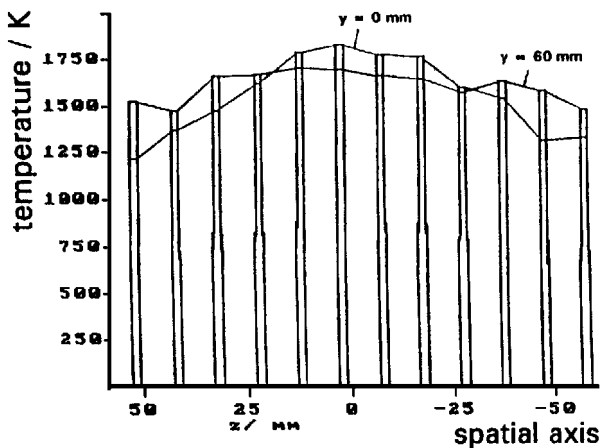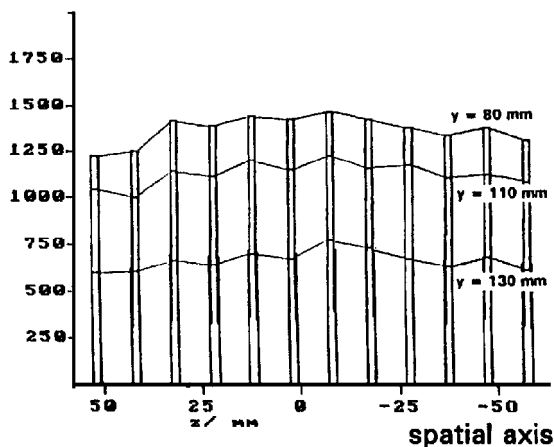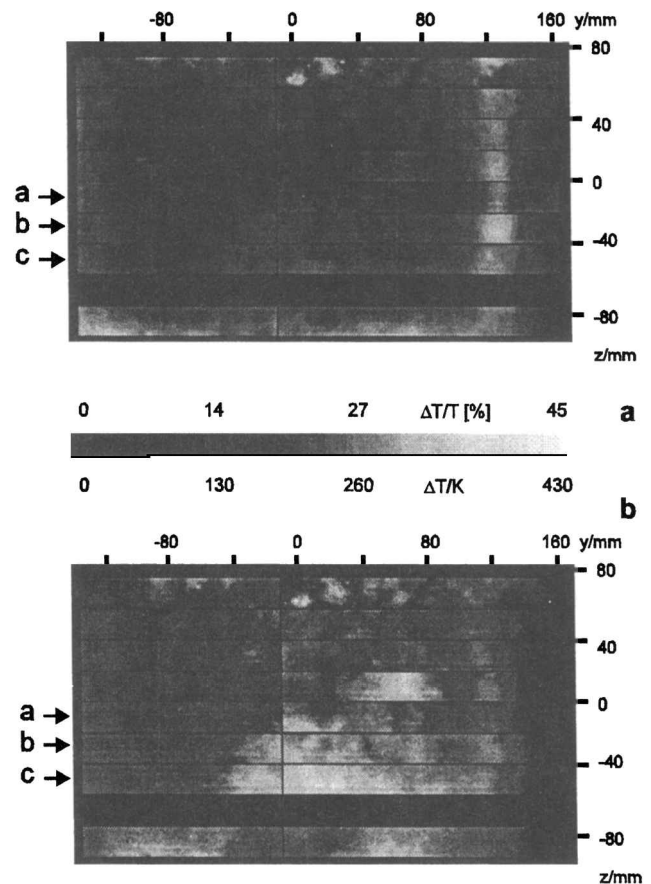
a) Horizontal



b) Vertical, *y* = 0 and 60 mm



c) Vertical, *y* = 80, 110, and 130 mm

**Fig. 13  Profiles of the corrected mean temperature field extracted from the data in Fig. 12.**



**Fig. 14   Spatial distribution of the variability of the temperature field at the burner exit: a) relative standard deviation $\sigma_T/T$, i.e., turbulence intensity and b) absolute standard deviation $\sigma_T$ in Kelvin.**

each detector element. The resulting image of the relative standard deviations (in percent), i.e., the turbulence intensity $\sigma_T / T$ is given in Fig. 14a and for the absolute standard deviations $\sigma_T$ (in Kelvin) in Fig. 14b, respectively. Fluctuations in the gas composition can cause errors in the single-shot temperature measurements, and this results in an error in the turbulence intensity distributions, but these are only discussed in a qualitative way here. These images are less reproducible using 50 single shots than the mean temperature field, but the main features, which will be discussed in the following, are repeatable. These images give an impression of the strength of turbulence as a function of the spatial position.

The zone where mixing of exhaust gas and ambient air occurred rendered high-temperature fluctuations. This zone can be seen particularly in Fig. 14a, especially on the lower and right-hand side. Obviously, the mixing zone has a waist near the vertical middle axis. This explains why a similar waist also occurred in the mean temperature field and in the majority species distributions (in particular, $H_2O$). It is reasonable to assume that cold ambient air is drawn into the freejet due to increased turbulence near the vertical middle axis.

It can be seen in Figs. 14a and 14b that the turbulence near the middle axis is stronger in the lower-half than in the upper-half, i.e., the turbulence distribution is asymmetric. This asymmetry in the turbulence distribution was also found by L2F (Laser 2 Focus) velocity measurements[12] done at DLR, German Aerospace Research Establishment. Other asymmetric structures within the exhaust gas area can be seen particularly in Fig. 14b. For example, the turbulence on the right-hand side tends to be stronger than on the left-hand side. These asymmetric structures are probably caused by a slight (unwanted) asymmetry in the hydrogen injection and burner geometry. The aforementioned vertical asymmetry can possibly also be explained by gravity (convection).

In conclusion, two-dimensional turbulence can be analyzed by the single-shot Rayleigh scattering technique. Note for this particular application that major features of the mean temperature field, especially the waist at the vertical middle axis, are caused by mixing of the turbulent freejet with ambient room air. These features are, therefore, not directly caused by the fuel injection or burner geometry, but due to spatially dependent turbulence structures. However, it is clear that the geometry of these turbulent structures is mainly dictated by the injection and burner geometry.

## Summary and Conclusions

Advanced two-dimensional Rayleigh scattering and one-dimensional Raman scattering laser techniques were applied to measure the temperature field and the distributions of the majority species,

H$_2$, O$_2$, H$_2$O, and N$_2$, at the burner exit of a H$_2$–air jet engine. The mean temperature field in the burner exit plane was derived from single-shot temperature images and turned out to be highly reproducible. The spatial turbulence distribution was also calculated from the single-shot temperature images. The majority species concentrations were used to correct the mean temperature field for spatial variations in the effective Rayleigh scattering cross section.

The turbulence intensity distribution $\sigma_T/T$ and the majority species distributions demonstrate that the structure of the mean temperature field was strongly affected by mixing of the turbulent free jet with ambient air, since the measurements were done 5 cm behind the open burner exit. No specific structure of the mean temperature field, for example, due to the hydrogen injection geometry, was observed. The mean temperature field is essentially symmetric with regard to both middle axes of the exit plane, whereas certain asymmetric structures were found in the turbulence and majority species distributions.

The majority species concentrations measured by one-dimensional Raman scattering showed that unburned H$_2$ occurred in certain regions in the burner exit plane that were essentially free of O$_2$ and vice versa. This pattern was essentially constant in time (over a long time scale), so that it could be observed by averaged measurements. This means that certain flow structures in the burner caused rich mixing in some areas and lean mixing in others, and this explains why overall combustion is not complete (about 75%) at the burner exit.

It is a major objective of future development to improve mixing in the burner to obtain overall complete combustion at its exit. Additional experiments would be helpful to elucidate the complete flowfield in the burner.

## Acknowledgments

## References

[1]Nandula, S. P., Brown, T. M., Cole, W. A., and Pitz, R. W., "Simultaneous Multi-Species Multi-Point Measurements in H$_2$–Air Flames Using a Narrowband KrF Excimer Laser," AIAA Paper 92-3348, July 1992.
[2]Reckers, W., Hüwel, L., Grünefeld, G., and Andresen, P., "Spatially Resolved Multispecies and Temperature Analyses in Hydrogen Flames," Applied Optics, Vol. 32, Feb. 1993, pp. 907–918.
[3]Grünefeld, G., Beushausen, V., Andresen, P., and Hentschel, W., "Spatially Resolved Raman Scattering for Multi-Species and Temperature Analysis in Technically Applied Combustion Systems: Spray Flame and Four-Cylinder In-Line Engine," Applied Physics B, Vol. 58, 1994, pp. 333–342.
[4]Cheng, T. S., Wehrmeyer, J. A., and Pitz, R. W., "Laser Raman Diagnostics in Subsonic and Supersonic Turbulent Jet Diffusion Flames," NASA CR 189544, Dec. 1991.
[5]Shirley, J. A., "UV Raman Spectroscopy of H$_2$–Air Flames Excited with a Narrowband KrF Laser," Applied Physics B, Vol. 51, No. 1, 1990, pp. 45–48.
[6]Smith, M., Smits, A., and Miles, R., "Compressible Boundary Layer Density Cross Sections by UV-Rayleigh Scattering," Optics Letters, Vol. 14, 1989, pp. 916–918.
[7]Shirinzadeh, B., Balla, J. R., Hillard, M. E., Anders, J. B., Exton, R. J., and Waiting, J. A., "Planar Rayleigh Scattering Results in Helium/Air Mixing Experiments in a Mach 6 Wind Tunnel," Applied Optics, Vol. 31, No. 30, 1992, pp. 6529–6534.
[8]Heinze, T., and Schmidt, T., "Fuel-Air Ratios in a Spray, Determined Between Injection and Autoignition by Pulsed Spontaneous Raman Spectroscopy," Society of Automotive Engineers, SAE Paper 892102, March 1989.
[9]Grünefeld, G., Beushausen, V., and Andresen, P., "Planar Air Density Measurements Near Model Surfaces by UV Rayleigh/Raman Scattering," AIAA Journal, Vol. 32, No. 7, 1994, pp. 1457–1463.
[10]Grünefeld, G., "Laser Diagnostics Applied to Practical Combustion and Flow Systems," Doctoral Dissertation, Univ. of Bielefeld, Cuvillier Verlag, Göttingen, Germany, Dec. 1994.
[11]Eckbreth, A. C., "Averaging Considerations for Pulsed, Laser Raman Signals from Turbulent Combustion Media," Combustion and Flame, Vol. 31, 1978, pp. 231–237.
[12]Mühleck, P., and Stursberg, K., "Fliegen mit Mach 7," DLR Nachrichten, Vol. 73, 1993, pp. 41–47.
[13]Andresen, P., Bath, A., Gröger, W., Lülf, H. W., Meijer, G., and Ter-Meulen, J. J., "Laser-Induced Fluorescence with Tunable Excimer Lasers as a Possible Method for Instantaneous Temperature Field Measurements at High Pressures: Checks with an Atmospheric Flame," Applied Optics, Vol. 27, No. 2, 1988, pp. 365–378.
[14]Grünefeld, G., Beushausen, V., and Andresen, P., "Interference-Free UV Laser-Induced Raman and Rayleigh Measurements in Hydrocarbon Combustion Using Polarization Properties," Applied Physics B, Vol. 61, 1995, pp. 473–478.

G. Laufer
*Associate Editor*